How 3D Printed Infill Patterns Affect Vibration

Joshua Towle
Glendale High School, 1440 E Broadway, Glendale, CA 91205, USA
jlt6412171@gmail.com
Tracy Lu
Polygence, Research Program Mentor
California Institute of Technology, PhD Candidate in Mechanical Engineering
tlu2@caltech.edu

Abstract

This research investigates how the internal geometry of 3D-printed parts, specifically infill patterns, influences their vibrational behavior. Focusing on cantilever beams, vibration was induced using a CNC spindle motor and measured with ADXL345 accelerometers to analyze damping ratios and natural frequencies. Four common infill patterns were tested, with data processed through FFT analysis, RMS calculations, and custom Python scripts. The findings provide insight into how internal structure affects vibration absorption and transmission, informing the design of lightweight 3D-printed components for machines, robotics, and other systems subject to dynamic loads.

Keywords: 3D-printing, vibration, damping, resonance, accelerometer, structural dynamics.

1. Introduction

3D printing has become an essential tool for producing complex geometries efficiently, enabling rapid prototyping for industries ranging from aerospace to robotics. A critical consideration in the design of these components is their dynamic behavior, particularly how they respond to vibration, which can influence structural integrity and performance under operating dynamics.

Vibrational analysis is especially relevant for components which can often be simplified and represented as cantilever beams, and are widely used in structural and mechanical systems. Although prior studies have explored parameter impacts, such as Doanay Kati et al. [3], who performed modal analysis on ABS cantilever beams considering the infill pattern, density, raster angle and nozzle size, and Oteyaka et al. [4], who examined damping differences across various PLA infill patterns and ratios, there remains a gap in comparing multiple common infill geometries under consistent test conditions. Work such as Papageorgiou et al. [5] highlights the role of composite materials and the shape of the infill in the vibration behavior, although not specifically within purely structural PLA cantilevers.

2. Overview:



Figure 1: ADXL345 accelerometer mounted on the 3D-printed cantilever.

Our study uniquely focuses on FDM-printed PLA cantilever beams with four standard infill patterns, measured by accelerometry and frequency domain analysis to quantify damping and resonance, allowing for optimization without altering exterior dimensions or mass (shown in Figure 1).

Vibrations were induced and measured using ADXL345 accelerometers to characterize damping behavior. These findings have implications not only for industrial applications—where optimizing vibration control can improve the performance and reliability of lightweight components—but also for hobbyists seeking structurally efficient and potentially vibration-resistant designs. Using frequency-domain analysis, RMS calculations, and custom Python scripts, this study systematically compares the dynamic characteristics of each pattern and offers guidance for future design optimization in robotics, assemblies of 3D-printed components, and other vibration-sensitive systems.

3. Methods / Experimental Setup

Accelerometer: Different hardware, sensors, and supporting materials were used for vibration testing, as well as the fixtures used to ensure accurate and repeatable measurements. To measure acceleration at the end of the cantilever beam, an ADXL345 accelerometer was used, as shown in Figure 2). As explained in Appendix A.1, the ADXL345 was chosen for its low cost and compatibility. The small form factor of the sensor makes it easy to mount directly on the 3D-printed cantilevers without significantly affecting their mass or dynamics. The ADXL345 also offers selectable measurement ranges up to $\pm 16\,g$ with 13-bit resolution. The accuracy of the sensor is discussed in Appendix A.2.

Microcontroller: The Arduino Uno (shown in Figure 3) was selected as the primary microcontroller for this experiment due to its accessibility, ease of use, and reliability for

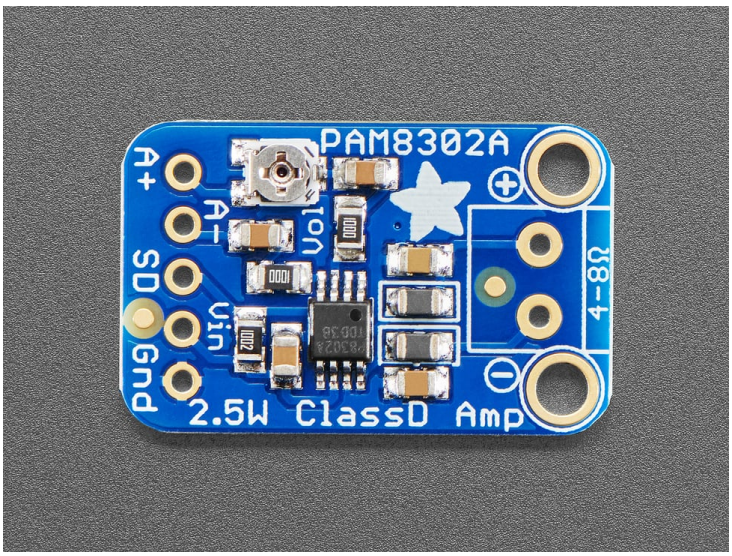


Figure 2: ADXL345 accelerometer.

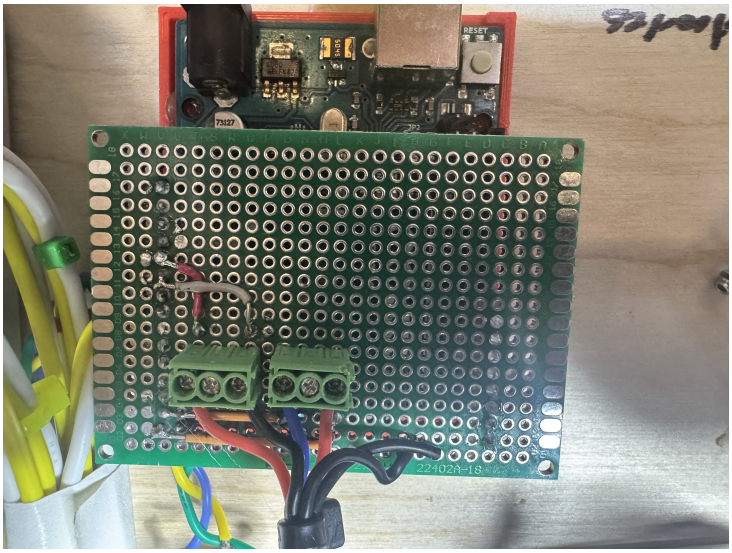


Figure 3: Custom Arduino Uno development board with terminal blocks for easy sensor connections.

rapid prototyping. Having multiple units readily available allowed for faster development and troubleshooting, reducing setup time for this project. The simple architecture of Arduino Uno and the well-supported ecosystem make both coding and wiring straightforward, particularly through the Arduino IDE. As explained in Appendix A.3, the Arduino provided a simple and reliable platform for sensor integration.

3D-printed cantilevers: The cantilevers used in this experiment were 3D printed from polylactic acid (PLA), a degradable thermoplastic widely considered one of the most common and accessible materials for the printing of fused filaments [6]. PLA was selected due to its low cost, ease of printing, and predictable mechanical properties, making it ideally suited for producing multiple identical samples under controlled conditions. Each cantilever was designed with dimensions optimized to balance two primary considerations: maximizing the number of specimens printable within the available time and 3D printer

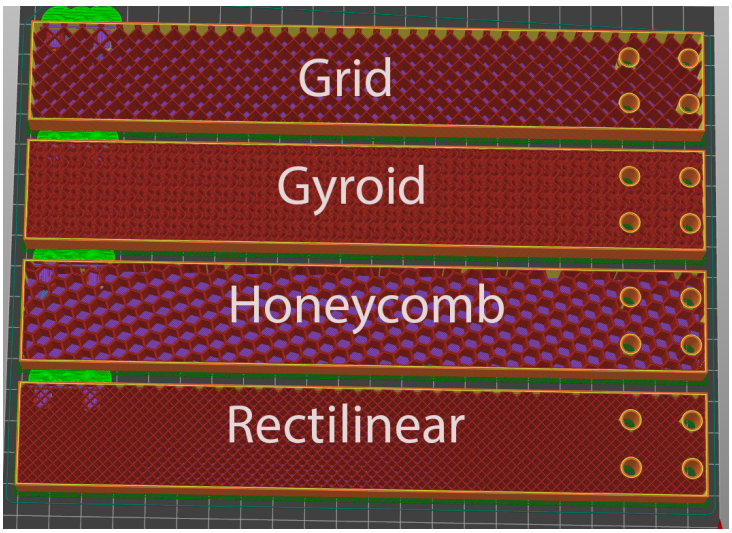


Figure 4: 3D-printed cantilever beams with four different infill patterns.

build volume, and ensuring sufficient length to amplify vibration amplitudes for reliable detection by the accelerometer.

A target mass of approximately 60 g was chosen for each beam, a value commonly used in structural infill studies to balance stiffness and weight [7], with actual printed masses ranging from 55.31 g to 55.67 g, yielding minimal variability ($\pm 0.18\,g$) among samples, as illustrated in Table 1. Four different internal infill patterns: rectilinear, gyroid, honeycomb, and grid (shown in Figure 4), were evaluated to determine their impact on vibrational behavior.

Table 1: Measured weights of 3D-printed cantilever specimens

Cantilever Name	**Weight (g)**
Rectilinear1	55.31
Gyroid1	55.67
Grid1	55.58
Honeycomb1	55.58

Range: 55.31 g to 55.67 g
Difference between heaviest and lightest: 0.36 g

Spindle CNC: The vibration source for the experiment was a compact CNC router spindle motor (RATTMMOTOR, 12–100 VDC, up to 16,000 RPM). This brushed DC motor is commonly used for small milling and engraving applications due to its compact form factor and stable high-speed performance. Its cylindrical aluminum housing facilitates straightforward mounting, while the integrated collet system allows for secure attachment of various tools or eccentric weights for vibration generation. The motor's wide voltage range and relatively low power requirements made it compatible with the test rig's portable power supply and control circuitry.

4. Mounting and Clamping Hardware

Iteration 1: Initial Design

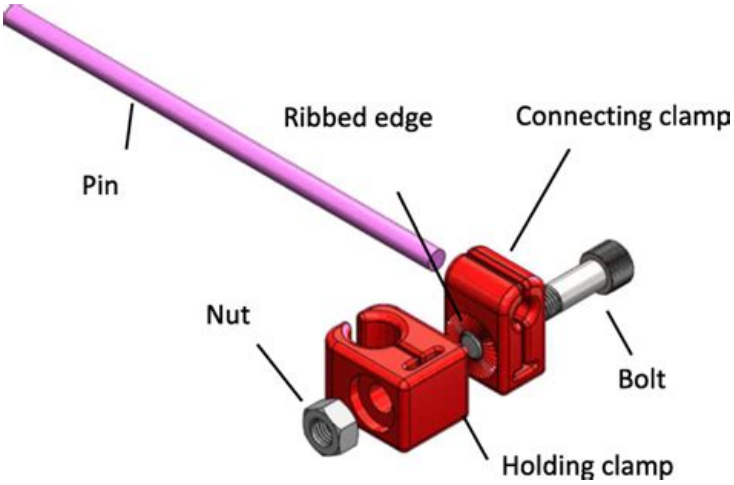


Figure 5: Original idea for cantilever mount.[1]

The first mounting design for the cantilever beams was adapted from a previous prototype [1] and relied on a single M4 screw with nut to clamp the beam between two PLA bracket arms (see Figure 5). The idea was to tighten the arms together, creating a friction fit on the beam. During testing, several deficiencies were observed. The spacing between the arms of the bracket was too wide, resulting in excessive play and poor beam alignment. This misalignment allowed movement during vibration testing, introducing inconsistencies in measured data. Additionally, tightening the bracket forced the PLA to flex around the beam, which weakened the structural integrity of both the beam and the mount over repeated tests. The single bolt also loosened over time due to cyclic loading, further compromising repeatability. This design did not conform to standard recommendations for cantilever mounting, which emphasize uniform clamping forces and minimal test deformation [2].

Iteration 2: Refined Design

The revised mount addressed the shortcomings of the first iteration by adopting a distributed clamping system. The new design uses four M4 bolts that pass through the cantilever arm. Sandwiched between the cantilever and the cantilever body are four rubber washers to minimize unwanted vibration. This provides a rigid, evenly distributed hold on the beam. This configuration allows quick replacement of cantilevers, which requires the removal of only four screws, while maintaining consistent boundary conditions between tests (see Figures 6 and 7). The bracket incorporates two 2mm thick legs that extend from its front and rear surfaces, allowing the bracket to be attached to a rigid work surface. Two C-clamps placed perpendicular to each other, approximately 5 inches apart, were used to fix the assembly to the table.

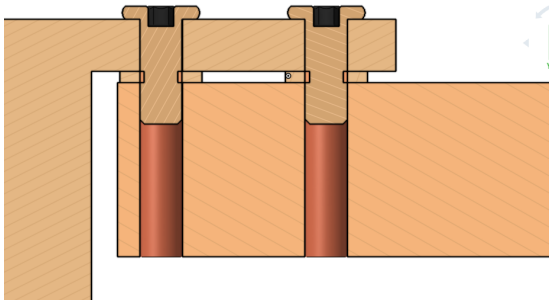


Figure 6: CAD rendering of the refined cantilever mounting system showing the distributed clamping design.

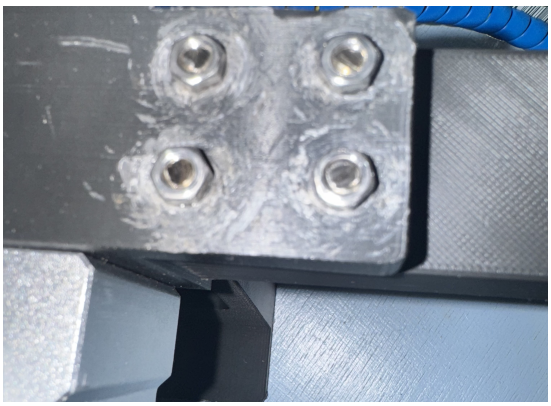


Figure 7: Photograph of the physical implementation of the refined mount, illustrating the installed bolts and bracket assembly.

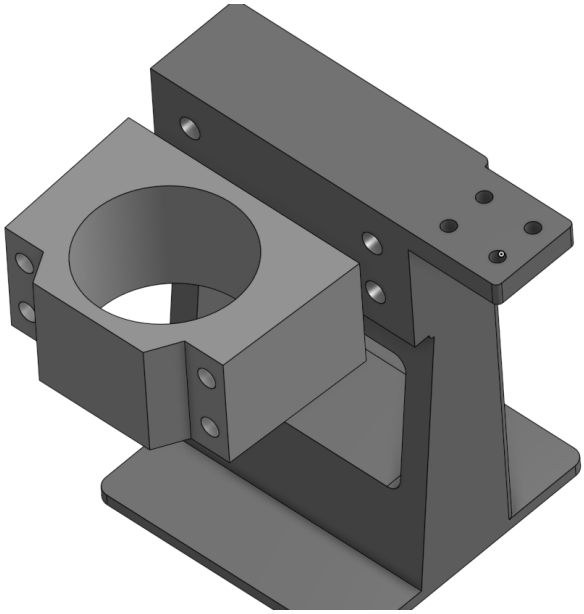


Figure 8: spindle motor fixture.

Vibration Induction and Isolation

Excitation of the cantilever beams was achieved using a CNC spindle motor mounted to a dedicated plate. The spindle housing was attached to the plate with four M4 heat-insert screws, ensuring rigid coupling and direct transfer of vibration to the cantilever (see Figure 8). To minimize transmission of unintended vibrations into the supporting table which could produce feedback or self-excited resonance, the base of the mounting assembly was lined with a 1.5mm thick toolbox-liner vibration mat. Damping materials of this type are widely used in machine tool applications to attenuate vibrations [9]. This addition effectively reduced extraneous noise and vibration in preliminary tests.

Sensor Mounting

The ADXL345 accelerometer was mounted to the free end of each cantilever using two M2 heat-insert screws, providing a secure and repeatable attachment that prevented sensor slippage without damaging the printed beam. This mounting ensured precise sensor alignment throughout all tests and minimized additional mass at the tip of the beam. The sensor was connected via a custom Arduino Uno development board equipped with terminal blocks for quick and reliable wiring changes between tests (see Figure 1).

Geometry and Sample Preparation

To isolate the effect of internal architecture, all beams shared the same outer geometry and mass to the extent practical. Each cantilever was printed in PLA with a fixed infill density of 20% (motivated by prior work balancing stiffness and dynamic response [4]) and identical exterior dimensions: length $L = 215\,\text{mm}$, width $b = 33\,\text{mm}$, and thickness $h = 20\,\text{mm}$. Beams were oriented so that bending occurred about the h dimension parallel to the width.

First-mode frequency (Euler–Bernoulli). For a uniform, slender cantilever, the first natural frequency is

$$f_1 = \frac{\beta_1^2}{2\pi}\sqrt{\frac{EI}{\rho A}}\,\frac{1}{L^2}, \qquad \beta_1 \approx 1.875, \tag{1}$$

with Young's modulus E, material density ρ, area A, and second moment of area I. For a rectangular cross-section,

$$I = \frac{b\,h^3}{12}, \qquad A = b\,h. \tag{2}$$

Numerical estimate for the selected geometry. Representative PLA properties (Young's modulus $E \approx 3.5$ GPa, density $\rho \approx 1.25\ \text{Mg/m}^3$) were taken from the Cambridge Materials Databook [8].

Using representative PLA properties (Young's modulus $E \approx 3.5\,\text{GPa}$, density $\rho \approx 1250\,\text{kg/m}^3$) and the chosen beam dimensions ($b = 33\,\text{mm} = 0.033\,\text{m}$, $h = 20\,\text{mm} = 0.020\,\text{m}$, $L = 215\,\text{mm} = 0.215\,\text{m}$):

$$I = \frac{0.033 \times (0.020)^3}{12} = 2.20 \times 10^{-8}\ \text{m}^4, \tag{3}$$

$$A = 0.033 \times 0.020 = 6.60 \times 10^{-4}\ \text{m}^2, \tag{4}$$

$$f_1 = \frac{(1.875)^2}{2\pi}\sqrt{\frac{(3.5\times10^9)\,(2.20\times10^{-8})}{(1250)\,(6.60\times10^{-4})}}\,\frac{1}{(0.215)^2} \;\approx\; 1.17\times10^2\ \text{Hz}. \tag{5}$$

So, the expected resonance is $\mathbf{f_1 \approx 117}$ Hz, which comfortably lies within the measurement bandwidth of the accelerometer used. B.2 shows the real meaning behind 117 Hz in our experiment.

Cantilever preparation and control. To minimize confounding factors:

- External dimensions (L, b, h) and nominal infill density (20%) were held constant across all beams; only the infill pattern varied (seen in Table 1).
- Each printed beam was inspected and lightly deburred to remove stray filaments; overall dimensions were verified with calipers and recorded.
- Mass was recorded to confirm comparability across specimens.
- The ADXL345 accelerometer was mounted at the free end (tip) of the cantilever with the same mounting process and dimensions to capture maximum response amplitude; cable routing was used to avoid strain.
- All tests used the same mount and tightening procedure to ensure repeatable boundary conditions at the clamp.

Rationale for $L = 215$mm. In the cantilever frequency equation, all parameters such as material stiffness, density, and cross-sectional geometry are fixed for our samples, leaving length as the only variable. This makes the reference frequency directly proportional to the inverse square of the length. By selecting a length of 215 mm, the resulting reference frequency of about 117 Hz falls within a clean, measurable range for the ADXL345 sensor, ensuring strong signal detection and good separation between infill patterns.

5. Data Acquisition and Processing

Data from each cantilever test was collected using a custom Python-based acquisition and analysis workflow. The system was designed to interface directly with the ADXL345 three-axis accelerometer, mounted at the free end of the beam, and record acceleration data for the duration of each test.

Sampling Configuration The ADXL345 was configured with a measurement range of $\pm 16\,g$, ensuring that peak accelerations during vibration were within the sensor's range. The output data was set to 570 Hz, to capture the full frequency content of the beam's response. The sampling frequency f_s describes how many data points are recorded per second. It can be found by measuring the time gap Δt between two consecutive readings from the sensor and taking the reciprocal:

$$f_s = \frac{1}{\Delta t}, \quad \Delta t = t_{i+1} - t_i$$

where t_i and t_{i+1} are the timestamps of two consecutive samples in seconds. For example, if each reading occurs every 0.0005 seconds, then $f_s = 2000$ Hz, meaning 2000 samples are recorded per second.

Data Acquisition Procedure During testing, the microcontroller (Arduino Uno) queried the ADXL345 over the I^2C interface at the configured sampling rate. For each sample, raw 16-bit integer values were read for the X, Y, and Z axes, converted to acceleration in g using the device sensitivity, and time-stamped in milliseconds relative to the start of acquisition. These values were streamed to the host computer and stored in comma-separated value (CSV) format, preserving all three acceleration components and the time index.

Data Storage and Organization Each test produced a single CSV file containing four columns: `time_ms`, `accel_x`, `accel_y`, and `accel_z`. Filenames were structured to encode the test type (forced or natural frequency), the infill pattern, and the trial number (e.g., `Cantilever_Gyroid_Natural_1.csv`), ensuring traceability during later analysis.

Data Processing Pipeline Post-processing was performed in Python using `pandas`, `numpy`, `matplotlib`, and `scipy`. The primary steps were:

1. **Preprocessing:** Remove any constant bias from each axis by subtracting the mean, and convert `time_ms` to seconds.

2. **RMS Calculation:** The root-mean-square acceleration for each axis was computed as

$$a_{\text{RMS}} = \sqrt{\frac{1}{N}\sum_{i=1}^{N} a_i^2}$$

   where N is the number of samples and a_i is the acceleration at sample i. The total RMS magnitude was calculated as

$$a_{\text{RMS,total}} = \sqrt{a_{x,\text{RMS}}^2 + a_{y,\text{RMS}}^2 + a_{z,\text{RMS}}^2}.$$

3. **FFT Analysis:** The one-sided Fast Fourier Transform (FFT) of each acceleration axis was computed using `scipy.fft.rfft` to obtain the frequency spectrum. The zero-frequency (DC) component was removed to focus on the stuff we wanted. The resonant frequency was seen as the frequency with the largest amplitude in the Y-axis spectrum.

4. **Damping Ratio Estimation:** For natural frequency decay tests, peaks in the Y-axis acceleration were identified and fit with an exponential decay function:

$$x(t) = Ae^{-bt} + C$$

   The decay constant b and the natural frequency f_n were then used to compute the damping ratio:

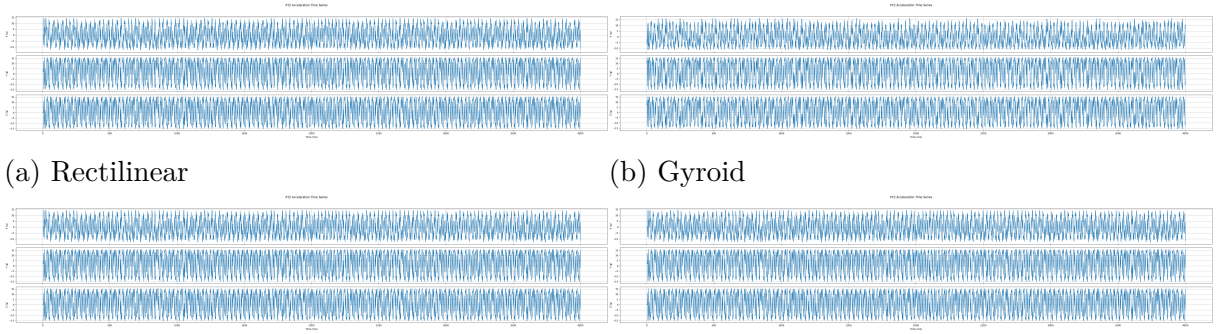
$$\zeta = \frac{b}{2\pi f_n}.$$

All intermediate and final results, including time histories, FFT plots, RMS comparisons, and damping ratios, were saved as PNG figures and CSV summary files for inclusion in the analysis and results sections.

6. Data Plots

Test A: Steady-State Forced Vibration

For the steady-state condition, the spindle was brought to its set speed and allowed to stabilize. Data collection then ran for 4,000 ms (4.0 s) while the vibration remained approximately constant (raw data seen in Figure 9). Spindle speed was measured with a handheld tachometer, and the motor was controlled via the external electronics box using a toggle switch. Importantly, excitation was only applied after the spindle reached full speed to avoid ramp-up transients contaminating the record.

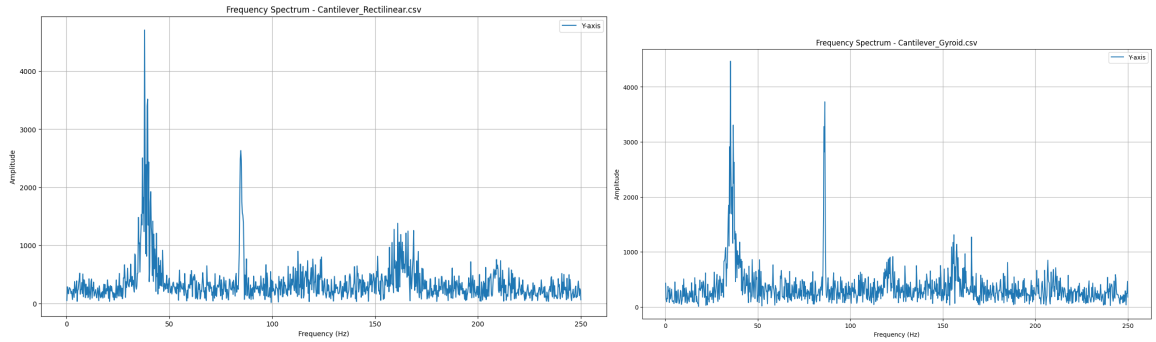


(a) Rectilinear (b) Gyroid

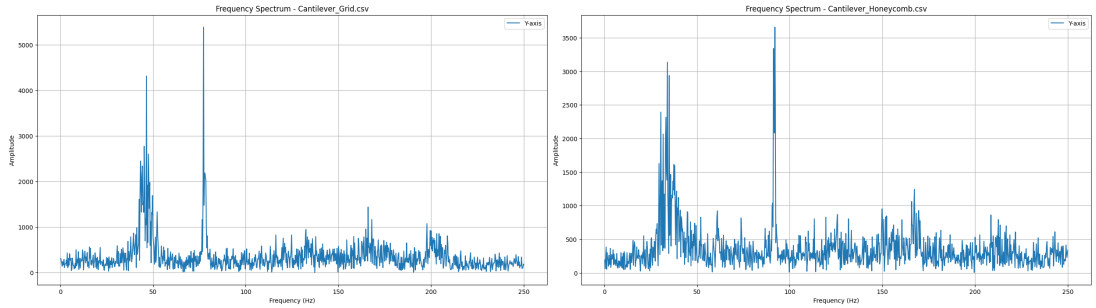
(c) Grid (d) Honeycomb

Figure 9: Forced vibration tests: XYZ acceleration vs. time for each infill pattern.

Figure 10 presents the Y-axis FFT magnitude for each 3D-printed cantilever infill pattern under natural frequency testing. In each plot, the tallest peak corresponds to the dominant resonant frequency of the beam's vibration response. While all patterns exhibit a primary frequency within a similar range, variations in peak height and the prominence of secondary peaks suggest differences in how each infill type stores and dissipates vibrational energy. These differences can be linked to stiffness and internal geometry, which influence both the frequency and amplitude of the response.



(a) Rectilinear (b) Gyroid



(c) Grid (d) Honeycomb

Figure 10: Forced vibration: Y-axis FFT magnitude spectra showing dominant frequency peaks for each infill pattern.

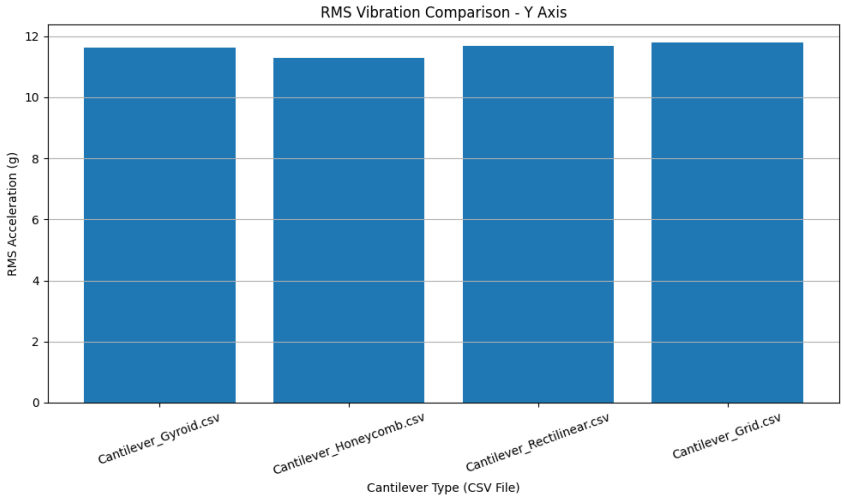
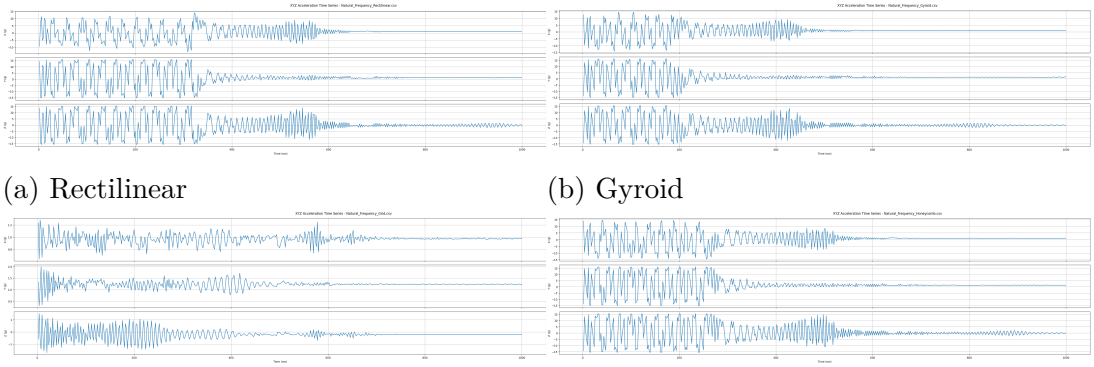


Figure 11: Forced vibration tests: RMS acceleration comparison for all infill patterns.

Figure 11 shows the root-mean-square (RMS) acceleration values measured along the Y-axis for each cantilever infill pattern under forced vibration. RMS acceleration represents the effective magnitude of the oscillatory motion over the test duration, providing a single value that captures both the amplitude and persistence of vibration. The results indicate that all infill patterns produced similar RMS levels, suggesting that under constant external excitation, the energy transmitted through the beam is relatively consistent regardless of internal geometry.

Test B: Natural-Response

For the natural-frequency–oriented condition, the spindle was first accelerated to its target speed (up to 15,000 RPM, as indicated by the tachometer). Acquisition began once full speed was reached; immediately at $t = 0$ the motor was switched off, and the system was recorded for 3,700 ms (3.7 s) as the spindle coasted down to rest. This procedure produces a broadband, decreasing forcing frequency that sweeps through the beam's resonances, while also capturing the decay of the structural response once external power is removed.



(a) Rectilinear (b) Gyroid

(c) Grid (d) Honeycomb

Figure 12: natural frequency vibration tests: XYZ acceleration vs. time for each infill pattern.

Figure 12 presents the raw acceleration time histories for all three measured axes (X, Y, and Z) across each infill pattern. The oscillations visible in each plot represent the beam's vibrational motion following the removal of external excitation, with amplitude gradually decaying due to damping. Differences in decay rate and waveform shape between patterns indicate how internal geometry influences the way stored vibrational energy is dissipated.

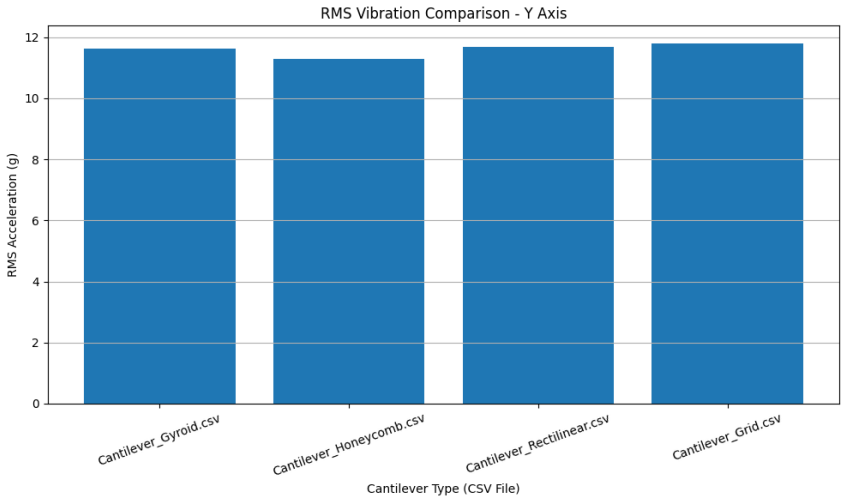
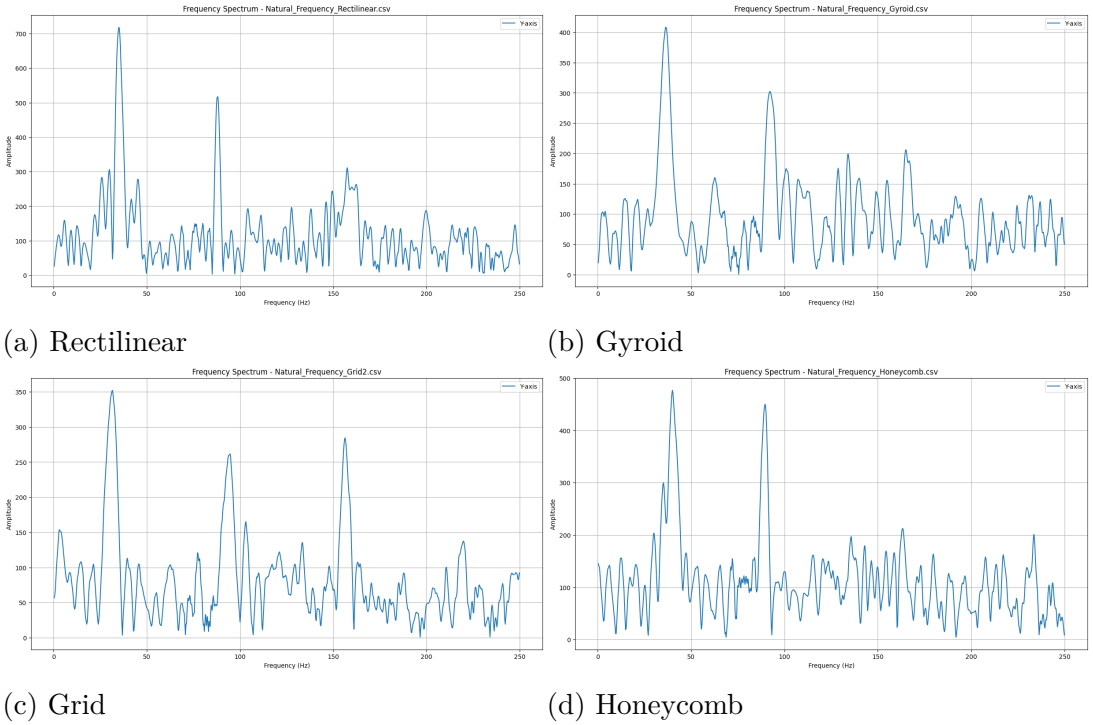


Figure 13: Natural Frequency tests: RMS acceleration comparison for all infill patterns.

The RMS acceleration values for the natural-frequency tests, shown in Figure 13, indicate relatively consistent vibration energy levels across all four infill patterns. Gyroid and rectilinear specimens exhibited the highest RMS accelerations, suggesting slightly

stronger sustained oscillations during the decay period, while Honeycomb showed the lowest value.



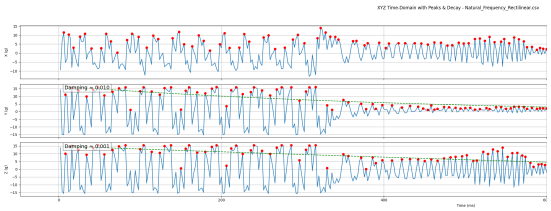
(a) Rectilinear (b) Gyroid

(c) Grid (d) Honeycomb

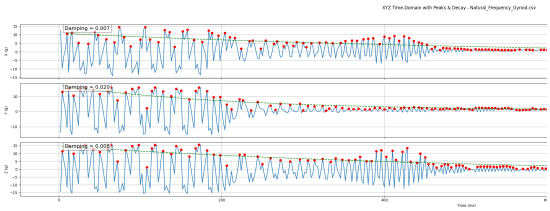
Figure 14: Natural frequency: Y-axis FFT magnitude spectra showing dominant frequency peaks for each infill pattern.

The FFT magnitude spectra (seen in Figure 14) for the natural frequency tests reveal distinct dominant peaks for each infill pattern, corresponding to the measured resonance frequencies. The Rectilinear beam exhibited its highest peak at approximately 34.93 Hz, while the Gyroid pattern resonated at 36.34 Hz. The Honeycomb pattern showed a slightly higher peak frequency of 40.00 Hz, and the Grid pattern demonstrated the highest resonant frequency at 83.10 Hz. These results indicate that infill geometry significantly influences the beam's stiffness and dynamic response, with the Grid configuration producing the stiffest structure and thus the highest natural frequency.

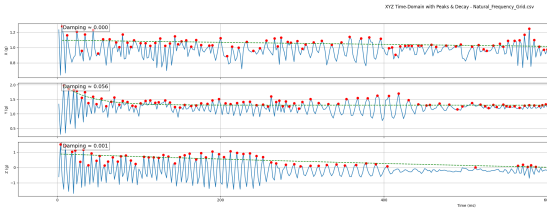
The damping ratio results (seen in figure 15) show clear differences between the infill patterns. The Grid pattern exhibits the highest Y-axis damping ratio ($\zeta \approx 0.056$), indicating that it dissipates vibrational energy more rapidly than the other patterns. The Gyroid pattern shows a moderate damping ratio ($\zeta \approx 0.020$), while the Rectilinear and Honeycomb patterns have the lowest values ($\zeta \approx 0.010$–0.011), meaning they sustain oscillations for a longer duration after excitation. These results suggest that the Grid infill is most effective in reducing vibration amplitude over time, whereas Rectilinear and Honeycomb infills are more prone to prolonged ringing once excited.



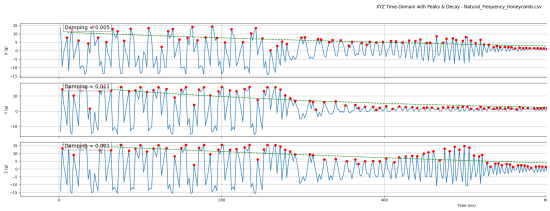
(a) Rectilinear



(b) Gyroid



(c) Grid



(d) Honeycomb

Figure 15: Natural frequency tests: Y-axis damping ratios for each infill pattern.

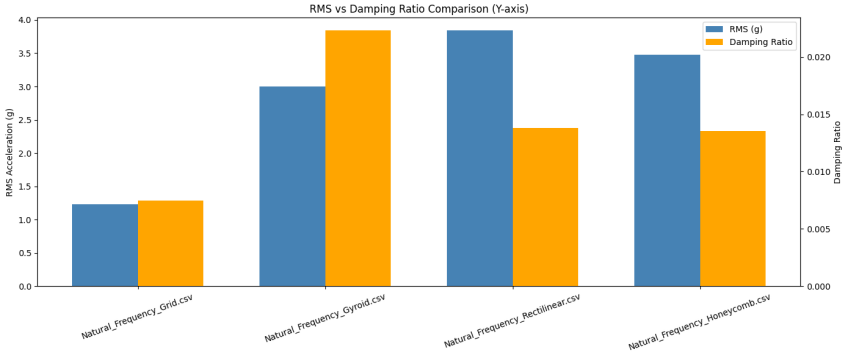


Figure 16: RMS acceleration and damping ratio comparison for each infill pattern under natural frequency tests.

The combined RMS acceleration and damping ratio results (seen in figure 16) provide insight into both the vibrational intensity and energy dissipation characteristics of each infill pattern under natural frequency excitation. The Gyroid and Rectilinear patterns produce relatively high RMS acceleration values, indicating stronger oscillations, with Gyroid also showing a moderate damping ratio. The Grid pattern has the lowest RMS acceleration but the highest damping ratio. The Honeycomb pattern exhibits moderate RMS acceleration and low damping, suggesting it sustains vibrations for longer durations compared to Grid but less than Rectilinear or Gyroid in terms of amplitude.

7. Results

Findings The Rectilinear beam exhibited a dominant resonant frequency of 34.93 Hz with a damping ratio of approximately 0.010, and produced the highest RMS acceleration at around 3.8 g. The Gyroid beam resonated at 36.34 Hz, with a damping ratio of about 0.020 and an RMS acceleration of roughly 3.0 g. The Honeycomb beam showed a resonant frequency of 40.00 Hz, with a damping ratio of approximately 0.011 and an RMS accelera-

tion near $3.5\,g$. The Grid beam demonstrated the highest resonant frequency at 83.10 Hz, with a damping ratio of about 0.012 and the lowest RMS acceleration at approximately $1.2\,g$.

8. Discussion

Overview Among the four tested patterns, grid fill stood out as producing the lowest RMS response and the highest natural frequency. This meant that it transmitted the least vibration amplitude. However, the damping ratio for the grid infill was the lowest, so vibrations continued once excited. Gyroid, on the other hand, showed the strongest damping effect, dissipating vibration energy the fastest, although it also exhibited higher oscillation amplitudes. Together, these results suggest that Grid is best when minimizing vibration response is the goal, while Gyroid is best when faster decay of vibration is more important. Honeycomb and Rectilinear were the least effective overall, as they both combined relatively high vibration amplitudes with poor damping, with Rectilinear performing worst.

Implications and Significance Many studies looked at how infill affects strength or weight theoretically, but fewer directly compared the vibration performance of common infills under the same conditions in practical testing scenarios. The findings of this study show that the fill geometry plays an important role in shaping the behavior of 3D-printed PLA beams when all other variables are constant. By showing how different infill patterns influence both resonance frequency and damping, our work highlights the potential to use internal structure as a design parameter for vibration control, not just for weight and stiffness optimization. The significance of this research is that engineers and designers can tailor 3D-printed components to meet specific performance needs: Grid infill to reduce vibration amplitude, gyroid infill to dissipate energy more rapidly, and, according to our study, people should be careful to avoid Rectilinear or Honeycomb infill when vibration resistance is critical.

limitations Although we tried to minimize sources of error, several factors may have affected the precision and accuracy of the data. The test setup included rubber washers between the bolts in the setups and a vibration mat to reduce environmental feedback, yet small amounts of unintended vibration from the table or motor housing may still have influenced the measurements. While all beams were printed to identical outer dimensions and weights, variations in layer inconsistencies and internal filament paths created by the infill patterns meant the specimens were not perfectly uniform, and so did not fully conform to theoretical assumptions. Finally, as with all FDM-printed PLA parts, small inconsistencies in the material or print quality could have contributed to imperfect results.

Additionally, we tried to keep the weight of the cantilevers the same, we had a small error of about 2%. This factor did not significantly affect our data acquisition and analysis.

The ADXL345 accelerometer introduces only a small error (±2% scale factor, ±0.35–1.5% zero-g offset, and ±2% cross-axis sensitivity), which is negligible compared to the large differences observed between infill patterns. C.1 shows more limitations we faced in the experiment in more detail.

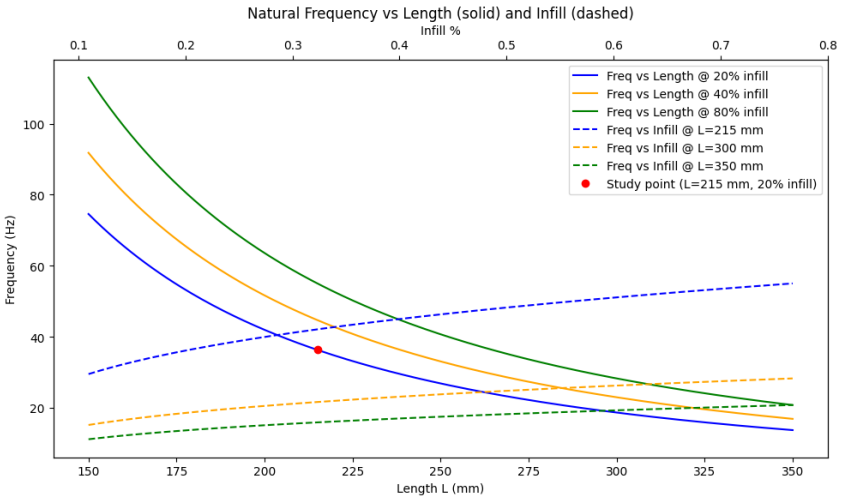


Figure 17: Natural frequency comparison across beam lengths and infill levels. Solid curves show frequency vs. length at different infill percentages, while dashed curves show frequency vs. infill at selected lengths. The red marker indicates the study condition (215 mm, 20% infill)

Recommendations In this study, we only tested beams at a length of 215 mm. For future research, it would be valuable to extend these tests to a broader range of lengths and fill percentages, for example 215 mm, 300 mm, and 350 mm. It is possible that the Rectilinear and Honeycomb infills performed poorly here simply because they were not tested under their optimal conditions. Longer beams generally shift the natural frequency lower, while higher infill makes parts stiffer (and heavier), influencing both frequency and damping. In addition, all beams in this study were limited to the same infill percentage, but future work could explore varying infill levels (e.g., 40%, 60%, 80%) to determine whether Rectilinear or Honeycomb become more effective under different geometric conditions. The 117 Hz solid-beam estimate could serve as a useful theoretical reference line for comparison. As shown in Figure 17, the theoretical frequency changes significantly as variables such as length and infill are adjusted, highlighting possibilities that were beyond the scope of this study. B.1 shows the derivation of the natural frequency scaling law used in the graph.

Closing Thought As 3D printing continues to expand into engineering and manufacturing, we must take advantage of these design freedoms to create components that are not only lightweight and strong, but also tuned to handle vibration in smarter, more efficient ways.

A. Appendix: Sensor and Electronics Details

A.1 Accelerometer Justification

The three-axis accelerometer is widely available at a low price, making it ideal for a project requiring multiple test samples, and its digital interface supports I^2C communication, allowing seamless connection with Arduino and ESP32 microcontrollers. The small form factor of the sensor makes it easy to mount directly on the 3D-printed cantilevers without significantly affecting their mass or dynamics. The ADXL345 also offers selectable measurement ranges up to ±16 g with 13-bit resolution.

A.2 Accelerometer Accuracy

The device has a noise density of approximately 220 $\mu g/\sqrt{\text{Hz}}$, providing sufficient accuracy (roughly ±0.05–0.1 g after calibration) to compare vibration energy between different infill patterns. In addition, the device is well documented, supported by numerous libraries and tutorials, and easily integrates into Arduino IDE for data analysis.

A.3 Arduino Justification

Arduino also integrates seamlessly with the ADXL345 accelerometer via I^2C, eliminating the need for complex interfacing hardware. Although more powerful microcontrollers are available, the Uno provided sufficient processing capability and memory to collect and transmit vibration data, making it a practical and efficient choice for this experimental setup.

B. Appendix: Calculations

B.1 Tie the equation to the graph

The observed trends in Figure 17 can be explained by the theoretical scaling law for natural frequency:

$$f(p, L) \propto \sqrt{\frac{p}{p_{\text{ref}}}} \left(\frac{L_{\text{ref}}}{L}\right)^2,$$

where p is the infill fraction and L is the beam length, with p_{ref} and L_{ref} serving as reference values. This relationship shows that frequency increases with the square root of infill (stiffer beams resonate faster) and decreases quadratically with length (longer beams resonate more slowly). The solid curves in Figure 17 demonstrate the effect of length variation at fixed infill percentages, while the dashed curves highlight how infill changes alter frequency at fixed lengths. For instance, increasing the beam length from 215 mm to 350 mm significantly reduces the predicted frequency, whereas raising the infill fraction from 20% to 80% shifts the frequency upward. This equation provides

the theoretical framework that underpins the recommendations for future experiments involving different beam lengths and infill levels, showing how changes in geometry and material distribution directly affect vibrational response.

B.2 Explaining data

The analytic estimate $f_1 \approx 117$ Hz comes from the Euler–Bernoulli cantilever formula

$$f_1 = \frac{\beta_1^2}{2\pi}\sqrt{\frac{EI}{\rho A}}\left(\frac{1}{L^2}\right),$$

using $I = bh^3/12$ and $A = bh$ for a *solid* rectangular beam. Our printed specimens, however, were only $\sim 20\%$ infill, so they are not solid. The internal voids reduce the *effective* area and, more importantly, the *effective* flexural stiffness $E_{\text{eff}} I_{\text{eff}}$. Although the mass density ρ_{eff} also decreases, the drop in stiffness dominates, so $\sqrt{(E_{\text{eff}} I_{\text{eff}})/(\rho_{\text{eff}} A_{\text{eff}})}$ is much smaller than for a solid beam. Consequently, the 117 Hz value should be viewed as a solid-beam upper bound; with 20% infill our measured first-mode frequencies fall near 30–40 Hz, which is consistent with the expected reduction in effective stiffness (and with added effects such as sensor mass and clamp compliance).

C. Appendix: Further limitations

C.1 Electronics

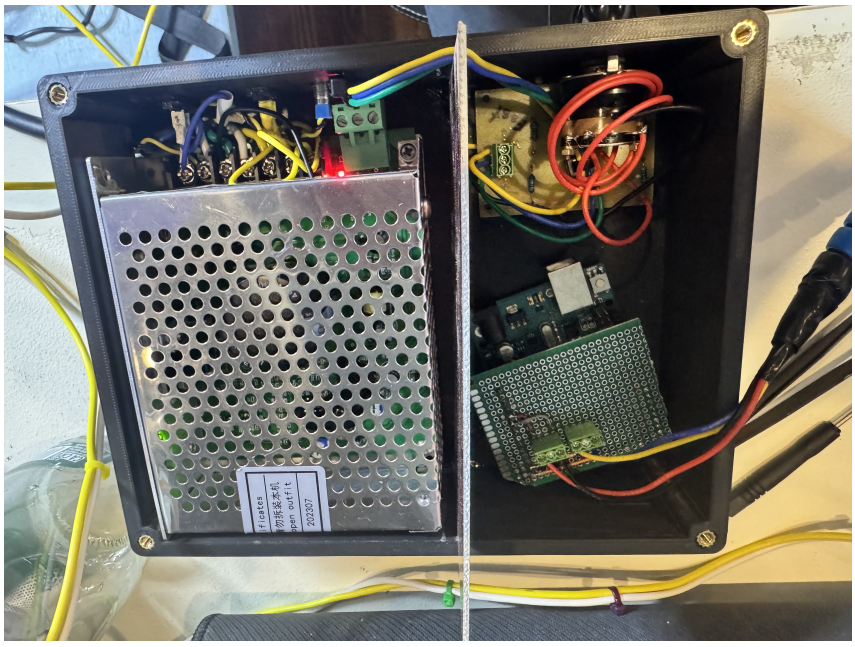


Figure 18: electronics box

Another limitation was a result of electromagnetic interference generated by the AC–DC converter powering the spindle motor. Because the converter was placed close to the

Arduino data acquisition board, it occasionally disrupted signal stability and sometimes corrupted measurements. To mitigate this, a copper plate was installed as a shield between the converter and the Arduino, with additional isolation at the container corners (seen in Figure 18). While this reduced the issue, it is possible that some residual interference introduced noise into the recorded data.

References

[1] Bidhan Bandyopadhyay, Bee-Ha Ang, and May Win Naing. "A review of computer-aided design/computer-aided manufacturing techniques for patient-specific 3D-printed implants". In: *3D Printing in Medicine* 6 (2020). Accessed 2025-08-17, p. 14. DOI: 10.1186/s41205-020-00084-3. URL: https://threedmedprint.biomedcentral.com/articles/10.1186/s41205-020-00084-3.

[2] IDC-Online. "Self-Excited Vibration Technical Note". In: *PMC/ScienceDirect* (n.d.). URL: https://www.idc-online.com/technical_references/pdfs/mechanical_engineering/Self_Excited_Vibration.pdf.

[3] Doganay Kati, Sinan Dalgic, and Mustafa Yavuz. "Experimental Modal Analysis of Fused Deposition Modeled ABS Cantilever Beams with Respect to Process Parameters". In: *Polymers* 17.12 (2025), p. 1615. DOI: 10.3390/polym17121615. URL: https://www.mdpi.com/2073-4360/17/12/1615.

[4] Barış Oteyaka, Erdem Ulu, and Yusuf Bozkurt. "Effect of Infill Pattern and Ratio on the Flexural and Vibration Damping Characteristics of FDM Printed PLA Specimens". In: *International Journal of Engineering Technologies* 8.3 (2022), pp. 211–220. URL: https://www.researchgate.net/publication/365321996_Effect_of_Infill_Pattern_and_Ratio_on_the_Flexural_and_Vibration_Damping_Characteristics_of_FDM_Printed_PLA_Specimens.

[5] Konstantinos Papageorgiou, Athanasios Kalogeras, and Dimitrios Tsikritzis. "Experimental Investigation of 3D-Printed Carbon-Fiber-Reinforced Composite Parts Manufactured with Different Infill Patterns". In: *Manufacturing and Materials* 9.2 (2025), p. 59. DOI: 10.3390/mmi9020059. URL: https://www.mdpi.com/2504-477X/9/2/59.

[6] ResearchGate. "PLA is widely used in 3D printing for its accessibility and mechanical predictability". In: *ResearchGate* (2018). URL: https://www.researchgate.net/publication/327976171_The_Effect_of_Three_Dimensional_Printed_Infill_Pattern_on_Structural_Strength.

[7] ScienceDirect. "Structural studies show 60% infill is commonly used for stiffness-weight optimization in PLA beams". In: *PMC/ScienceDirect* (2020). URL: https://pmc.ncbi.nlm.nih.gov/articles/PMC9862055/.

[8] University of Cambridge, Department of Engineering. *Materials Databook*. Accessed 2025-08-09. 2003. URL: http://www-mdp.eng.cam.ac.uk/web/library/enginfo/cueddatabooks/materials.pdf.

[9] Author Unknown. "Analysis of Vibration Damping in Machine Tools". In: *ResearchGate* (n.d.). Accessed: 2025-08-05. URL: www.researchgate.net/publication/326838019_Analysis_of_Vibration_Damping_in_Machine_Tools.